Jinst

Published by IOP Publishing for Sissa Medialab

Received: *November 29, 2022*
Accepted: *December 31, 2022*
Published: *April 7, 2023*

Inductively-coupled plasma discharge for use in high-energy-density science experiments

C.D. Arrowsmith,[a,*] **A. Dyson,**[a] **J.T. Gudmundsson,**[b,c] **R. Bingham**[d,e] **and G. Gregori**[a]

[a] *Department of Physics, University of Oxford, Parks Road, Oxford OX1 3PU, U.K.*
[b] *Science Institute, University of Iceland, Dunhaga 3, IS-107 Reykjavik, Iceland*
[c] *Space and Plasma Physics, School of Electrical Engineering and Computer Science, KTH Royal Institute of Technology, SE-100 44, Stockholm, Sweden*
[d] *STFC Rutherford Appleton Laboratory, Chilton, Didcot OX11 0QX, U.K.*
[e] *Department of Physics, University of Strathclyde, Glasgow G4 0NG, U.K.*

E-mail: charles.arrowsmith@physics.ox.ac.uk

Abstract: Inductively-coupled plasma discharges are well-suited as plasma sources for experiments in fundamental high-energy density science, which require large volume and stable plasmas. For example, experiments studying particle beam-plasma instabilities and the emergence of coherent macroscopic structures — which are key for modelling emission from collisionless shocks present in many astrophysical phenomena. A meter-length, table-top, inductive radio-frequency discharge has been constructed for use in a high-energy density science experiment at CERN which will study plasma instabilities of a relativistic electron-positron beam. In this case, a large volume is necessary for the beam to remain inside the plasma as it diverges to centimeter-scale diameters during the tens-of-centimeters of propagation needed for instabilities to develop. Langmuir probe measurements of the plasma parameters show that plasma can be stably sustained in the discharge with electron densities exceeding 10^{11} cm^{-3}. The discharge has been assembled using commercially-available components, making it an accessible option for commissioning at a University laboratory.

Keywords: Plasma generation (laser-produced, RF, x ray-produced); Plasma diagnostics - probes

*Corresponding author.

https://doi.org/10.1088/1748-0221/18/04/P04008

Contents

1 **Introduction** 1

2 **Two-coil inductively-coupled discharge** 2

3 **Measurements of the plasma parameters** 4

4 **A global volume-averaged model** 6

5 **Summary** 9

1 Introduction

Inductively-coupled plasma (ICP) discharges were first discovered more than a century ago [1–4], and the technology has been extensively-developed for a range of applications from light sources [5] to plasma propulsion [6], but in particular it is utilized within the semiconductor manufacturing industry for plasma-aided fabrication of integrated circuits [7, 8]. In an ICP, large volume plasmas are generated as energy is coupled into an ionized gas from a radio-frequency (RF) power source using an inductive circuit element (such as helical coil) positioned near-to, or immersed in, a discharge region [9, 10]. The ICP is therefore an electrodeless discharge that exists in various forms, including cylindrical geometry (solenoid) [11], planar geometry (flat spiral antenna) [7, 12], re-entrant geometry (the inductor is placed inside an inner glass cylinder) [13], as well as in ferrite immersed constructions [14, 15]. The cylindrical configuration in its simplest form is a gas filled tube made of quartz or ceramic placed inside a solenoid (the primary coil) through which RF current is applied.

The inductively coupled discharge in the cylindrical configuration has been explored extensively through the years [16], early on there was a debate on the workings of the discharge [2, 17], which was resolved in the late 1920s [18]. A transformer model of its operation was developed in the 1930s [19], and it has been characterized extensively experimentally over the past few decades [20–22]. The cylindrical ICP has been introduced to number of applications, including as a plasma torch in the 1960s [23], which has been applied in materials processing for decades; for plasma propulsion [6]; and is often applied as a remote plasma source in atomic layer deposition [24, 25].

The breakdown of a low pressure gas in the discharge region occurs because large RF currents in the coils lead to RF magnetic flux that penetrates within a skin depth layer of the gas. Electric fields are induced, which generate and sustain the plasma discharge as free electrons in the discharge are accelerated, and thermalize with the bulk gas via collisions to form a partially ionized plasma discharge. Typical ratios of electron number density to neutral atom number density are $\chi = n_e/n_n \approx 0.1$–$1\%$.

Using a 1-kW commercially-available power unit, supplying RF power at 13.56 MHz, it is possible to produce plasmas with electron densities exceeding 10^{11} cm^{-3} and dimensions exceeding

2023 JINST 18 P04008

meter-length and several centimeters in diameter. This makes ICPs well-suited to experiments in high-energy density science which require large, stable plasma. Here, we present an ICP discharge based on the cylindrical configuration which will be used in an experiment at CERN's HiRadMat facility [26, 27] to study convective beam-plasma instabilities of a relativistic electron-positron beam. In this case, a sufficiently-large volume is necessary for the beam to remain inside the plasma as it diverges to centimeter-scale diameters during the tens-of-centimeters of propagation needed for instabilities to develop. Such beam-plasma instabilities are studied in a range of contexts, for example, the magnetic field generation observed during current filamentation instabilities [28–30] of relativistic charged particle beams. The current filamentation can lead to self-generated emission of synchrotron radiation and has been proposed to play a role in the radiative emissions from collisionless shocks in energetic astrophysical outflows, such as those resulting in Gamma-Ray Bursts [31, 32].

In this paper, we describe the design of the plasma discharge, an inductively coupled discharge in the cylindrical configuration and its basic characterization. We present Langmuir probe measurements which have been used to determine the electron density, the electron temperature, the ion density, and the electron energy distribution function (EEDF) of the plasma. The electron energy distribution functions are found to be approximately Maxwellian, with temperatures of approximately $T_e \approx 4\,V$. In the text we sometimes use the roman typeface symbol T for the voltage equivalent of the electron temperature. Electron and ion densities are measured to exceed $10^{11}\,cm^{-3}$, corresponding to ionization fractions of $\chi = 0.5\%$.

2 Two-coil inductively-coupled discharge

A schematic of the design of the ICP discharge is shown in figure 1, and a photograph taken during operation is shown in figure 2. The device consists of a vacuum chamber comprised of three six-way port crosses separated by two sections of glass tube. The inductive elements are two helical coils made of copper piping, supplied by RF power in parallel via an impedance matching network. The coils are made of 1-cm diameter copper pipe with $8\frac{1}{2}$ turns and coil-winding inner diameter 7.5 cm. They wrap around 15-cm length sections of glass tubes, and power is inductively-coupled into the discharge gas across the glass boundary. The port-crosses, which are made from 304L-grade stainless steel, provide places where vacuum pumps, gas lines, and experimental diagnostics can be attached. The metallic parts of the chamber are all connected to a zero ground potential. In the planned experiment at HiRadMat, beams of electrons, positrons and protons enter through a glassy carbon window on the left port-cross and travel along the discharge tube.

The total length of the discharge region is $L = 87\,cm$, and the internal diameter is $d = 3.5\,cm$. The modular nature of the design makes it simple to extend the length of the discharge region. Before operation, the chamber is evacuated and maintained at a base pressure lower than 5 mPa. Argon gas is chosen as the operating gas as it is inert, inexpensive, and it has been well-studied for ICPs used in plasma materials processing, but other gases or gas mixtures can be used depending on the specific applications. A similar setup, an inductively coupled discharge in cylindrical geometry, composed of a quartz tube and a single helical coil, operated in pure hydrogen or H_2/Ar mixture has been applied to hydrogenate semiconductors [33, 34].

Power is supplied to the solenoid coils at a frequency of 13.56 MHz using a commercially-available radio-frequency power generator (Advanced Energy CESAR 1310), which can sustain a

2023 JINST 18 P04008

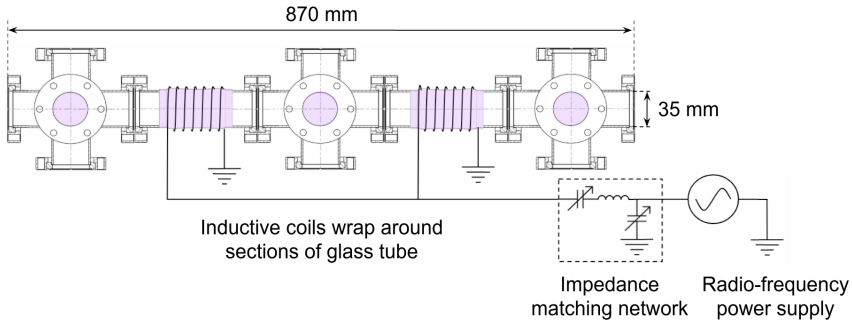

Figure 1. Schematic of the design of the inductively-coupled plasma discharge, which is composed of two inductive coils wrapped around sections of glass tube. The glass tubes are separated by port-crosses, incorporated into the design to allow diagnostics to be inserted. The coils are connected in parallel to a radio-frequency power source via an impedance matching network. The generated plasma extends between the coils along the full length of the vessel.

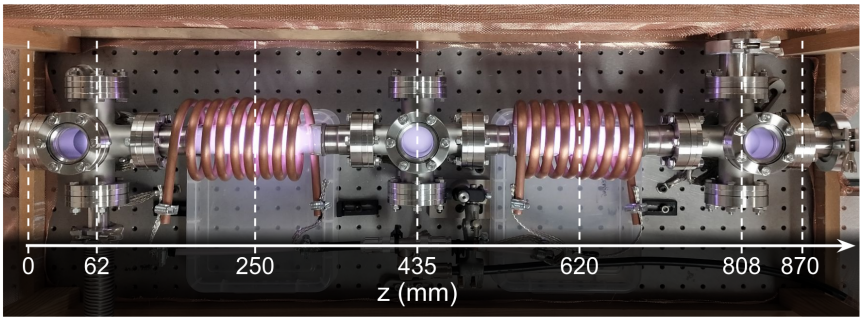

Figure 2. Photograph demonstrating the operation of the ICP discharge (imaged with the lid of the Faraday cage removed). The self-emission of the argon plasma can be seen, showing the plasma extending along the full length. A co-ordinate axis is added to show the axial positions that the Langmuir probe measurements correspond to in section 3.

power output of up to 1000 W. The power supply is attached to the coils via an impedance-matching network (Advanced Energy Navio), which minimizes the reflected power due to impedance mismatch.

The net power absorbed by the plasma is given by

$$P_{\text{abs}} = P_{\text{inc}} - P_{\text{ref}} - P_{\text{loss}} \tag{2.1}$$

where P_{inc} and P_{ref} are the forward and reflected power of the RF generator, and $P_{\text{loss}} = I_{\text{rms}}^2 R_{\text{eff}}$ are the losses due to ohmic heating in the coupling circuit. I_{rms} is the root mean square (RMS) current flowing through the coupling circuit, measured by a current probe mounted between the coils and the matching network, and R_{eff} is the effective resistance of the coupling circuit measured in the absence of a plasma (when the chamber is evacuated to the base pressure). The power coupling efficiency given by

$$\eta = \frac{P_{\text{abs}}}{P_{\text{inc}} - P_{\text{ref}}} \times 100\% \tag{2.2}$$

is measured to be approximately 25%.

2023 JINST 18 P04008

During operation, large RF potentials are generated on the structure and the coils, leading to capacitive coupling of power into the discharge. A weak, capacitively coupled (E mode) discharge is observed along the entire length of the tube at relatively low absorbed powers of $P_{\mathrm{abs}} = 20\,\mathrm{W}$. If $P_{\mathrm{abs}} \gtrsim 125\,\mathrm{W}$, and the operating pressure $p_{\mathrm{g}} \gtrsim 0.7\,\mathrm{Pa}$, a sudden increase in the luminosity and density of the plasma is observed. This signals the beginning of inductive coupling of power into the plasma (H mode). In an inductive mode of operation, plasma density is highest in the centre of the coils, exceeding $10^{11}\ \mathrm{cm}^{-3}$. The transition from E mode to H mode in the cylindrical ICP discharge is a well known phenomenon [8, 18] that has been explored over the years using e.g. a Langmuir probe [20] and through optical emission spectrometry [21]. The plasma density decreases in the discharge region outside of the coils, but due to the additional capacitive coupling of RF power into the gas, plasma is maintained along the entire tube with electron densities greater than $10^{10}\ \mathrm{cm}^{-3}$. The radial density profile of the plasma does not change significantly over the 3.5-cm diameter, but density along the central axis depends strongly on the position relative to the coils. In section 3, measurements are presented of the axial density profile when the discharge is operating in an inductive mode.

The plasmas generated are stably-sustained indefinitely. But in practice, the running time is limited to several minutes to prevent excessive heating of the coaxial cabling connecting the coils to the power unit.

3 Measurements of the plasma parameters

We use a commercially-available Langmuir probe unit (manufactured by Impedans, Ireland), which consists of a probe tip (a thin cylindrical tungsten wire with length 4 mm and radius 0.195 mm), and a RF compensation electrode. The probe tip holder is an alumina tube with radius 2 mm at the end of a probe shaft which contains RF chokes and connects to a data acquisition unit outside of the vacuum chamber. The probe tip is inserted into a plasma and is biased with a sawtooth voltage applied over a range between −50 V and +50 V. The measured probe current as a function of bias voltage (the $I - V$ probe characteristic) is used to determine the electron density (n_{e}), the ion density (n_{i}), the electron temperature ($\mathrm{T_e}$), and the EEDF ($g_{\mathrm{e}}(\mathcal{E})$).

When large negative voltages are applied to the probe tip, electrons are repelled by the negative sheath surrounding the probe tip and only positive ions are collected. This is named the ion-saturation region, and to obtain the ion number density and separate the contributions to the probe characteristic from ions and electrons, we fit empirical models of ion collection based on theories proposed by Laframboise [35] and Narasimhan [36] (LAF), and Allen, Boyd and Reynolds [37] and Klagge [38] (ABR).

Subtracting the ion contribution from the probe characteristic leaves us with the electron current I_{e}. In the region of the probe characteristic between electron and ion saturation, electrons with energy equivalent to the temperature of the distribution can reach the probe but lower-energy electrons are still repelled. The electron current can be fit in this region to obtain the electron temperature using

$$I_{\mathrm{e}} = I_{\mathrm{s}} \exp\left(\frac{V - V_{\mathrm{s}}}{\mathrm{T_e}}\right), \tag{3.1}$$

where V_{s} is the potential above which the electron current saturates, the plasma potential (identified by a maximum in $\mathrm{d}I_{\mathrm{e}}/\mathrm{d}V$). I_{s} is the current collected when the probe tip is at the plasma potential

2023 JINST 18 P04008

V_s. Once the electron temperature has been determined, the electron density is obtained using

$$n_e = \frac{I_s}{A_p}\left(\frac{2\pi m_e}{e^2 k_B T_e}\right)^{1/2}, \tag{3.2}$$

where A_p is the surface area of the probe tip, and m_e is the electron mass.

This analysis is valid provided the electron energy distribution function is Maxwellian. In the case where the EEDF is not Maxwellian, it can still be obtained via the Druyvesteyn formula [10, 39] which relates the EEDF to the second derivative of the electron current

$$g_e(\mathcal{E}) = \frac{2m_e}{e^2 A_p}\left(\frac{2eV}{m_e}\right)^{1/2}\frac{\mathrm{d}^2 I_e}{\mathrm{d}V^2}, \tag{3.3}$$

where $\mathcal{E}$ is the electron energy in equivalent voltage units. Electron density can be determined from the EEDF via

$$n_{e,\mathrm{eff}} = \int_0^\infty g_e(\mathcal{E})\mathrm{d}\mathcal{E}, \tag{3.4}$$

and the effective electron temperature T_{eff} by

$$T_{eff} = \frac{2}{3}\langle\mathcal{E}\rangle = \frac{2}{3}\int_0^\infty g_e(\mathcal{E})\mathcal{E}\mathrm{d}\mathcal{E}. \tag{3.5}$$

In the case where $g_e(\mathcal{E})$ is Maxwellian, the effective electron temperature T_{eff} is equal to T_e. Often the electron energy probability function (EEPF) is plotted $g_p(\mathcal{E}) = \mathcal{E}^{-1/2}g_e(\mathcal{E})$, and a Maxwellian electron energy distribution appears as a straight line.

The accuracy of the electron density and electron temperature when obtained using eq. (3.4) and eq. (3.5) is limited by the error in the shape of the EEDF arising from the digital smoothing of the data. Smoothing is necessary to obtain reasonable second-derivatives via numerical differentiation. A Blackman window has been found to achieve the most smoothing with minimal distortion of the IV-characteristic when applied to datasets subjected to artificial noise [40]. Given that the EEDFs we measure resemble Maxwellian distributions, the values we present for n_e and T_e use eq. (3.1) and eq. (3.2), since these are not subjected to distortions in the EEDF which arise in the process of smoothing. The agreement between the values obtained via eq. (3.1) and eq. (3.2) with those obtained via the two methods is quantified by calculating the mean of the relative differences between the measured values:

$$\frac{1}{N}\sum_{j=1}^{N}\left(\frac{|T_e - T_{eff}|}{T_e}\right)_j = 0.11, \qquad \frac{1}{N}\sum_{j=1}^{N}\left(\frac{|n_e - n_{e,\mathrm{eff}}|}{n_e}\right)_j = 0.12. \tag{3.6}$$

The differences do not tend to differ by more than $\sim 10\%$ of the measured value. This, combined with the errors from the fits, gives the presented errors in the measurements of T_e and n_e.

An example of some raw Langmuir probe data is shown in figure 3, taken when operating pressure is $p_g = 1$ Pa and absorbed power is $P_{abs} = 200$ W. The floating potential (where electron and ion current are net-zero) is marked, as is the space potential (where $\mathrm{d}^2I/\mathrm{d}V^2 = 0$ and $V > V_s$ signals electron saturation). The insets show fits of the ion and electron current used to obtain n_i, n_e and T_e.

2023 JINST 18 P04008

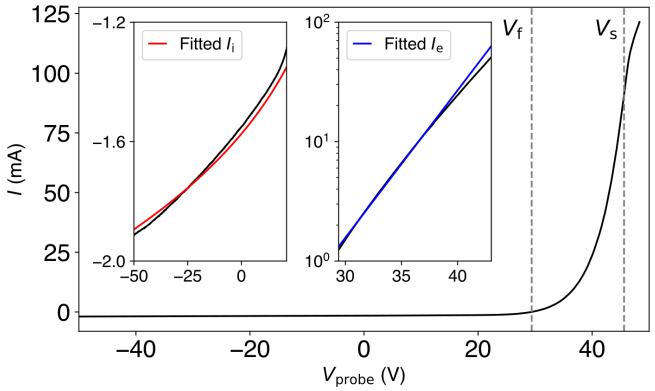

Figure 3. An example of raw Langmuir probe data ($I-V$ characteristic) taken with $p_g = 1$ Pa and $P_{abs} = 200$ W. The floating potential $V_f = 29.4$ V, and space potential $V_s = 45.6$ V, are labelled. The left-hand inset shows the fit of ion current, I_i, in the ion-saturation region used to obtain n_i (red). The right-hand inset shows the fit of electron current, I_e, in the transition region used to obtain n_e and T_e (blue).

Figure 4 shows the plasma parameters measured using this analysis for different axial positions probed along the discharge for a range of absorbed power $P_{abs} = 140 - 225$ W, when the operating pressure is $p_g = 1$ Pa. A correction factor has been applied to the electron density of $(1 + r_h/\lambda_e)$, where r_h is the radius of the probe holder, and λ_e is the electron mean free path [41]. This is to account for an under-estimation of the electron density arising from the depletion of electron density due to the probe holder.

In figure 4 (a)–(c), data is plotted from the centre of one of the outer-crosses to the centre of one of the coils. This represents a scan between the minimum and maximum of plasma density. In figure 4(d), the EEPFs are plotted for different axial positions in the case that $P_{abs} = 225$ W. They appear as straight lines, which indicates Maxwellian electron energy distributions. At all positions, the electron and ion densities are well-matched. Outside of the coils, the electron and ion density is $n = 10^{10}$ cm^{-3}. The maximum densities of 5×10^{11} cm^{-3} are found in the centre of the coil when $P_{abs} = 225$ W. The peak plasma density scales approximately linearly with the power absorbed by the plasma. Electron temperatures consistently lie in the range 3–5 eV.

Figure 5 shows how the plasma parameters measured at the central cross compare with those at the outer cross. We do not measure significant differences between the plasma conditions in the two positions.

4 A global volume-averaged model

The plasma parameters of the inductively coupled discharge, the electron density and the electron temperature can be estimated using a volume average global model [9, 10, 42]. The global model assumes a cylindrical discharge chamber (a dielectric tube) of radius R and length ℓ. At pressures for which the ion loss velocity is the Bohm velocity u_B, the overall discharge power balance for a cylindrical plasma discharge is written

$$P_{abs} = e n_0 u_B A_{eff} \mathcal{E}_T \tag{4.1}$$

2023 JINST 18 P04008

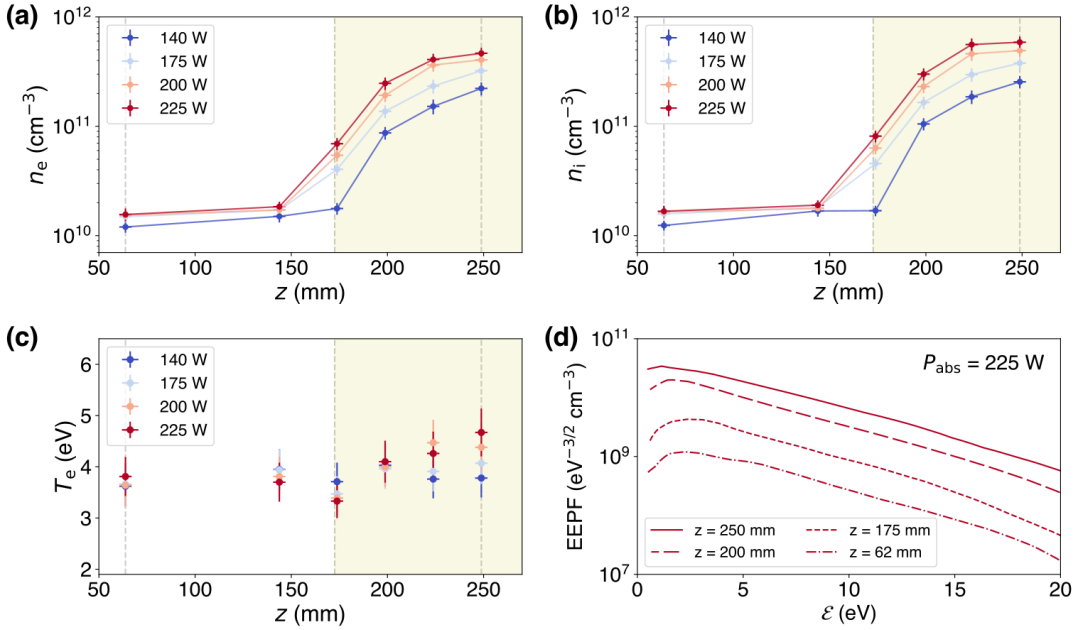

Figure 4. Langmuir probe measurements are used to obtain the (a) electron density, (b) ion density, (c) electron temperature, and (d) electron energy probability function (EEPF), at different axial positions, z, along the discharge for a range of absorbed powers (P_{abs} = 140 – 225 W), with an operating pressure p_g = 1 Pa. The vertical dashed lines correspond to: the centre of the outer cross (z = 62 mm), the edge of the inductive coil (z = 175 mm), and the centre of the inductive coil (z = 200 mm). The discharge region inside the coil is shaded yellow. At all positions, n_e and n_i are matched, being approximately 10^{10} cm^{-3} outside of the coils, and peaking at 5×10^{11} cm^{-3} in the coil centre when P_{abs} = 225 W. Electron temperatures consistently lie in the range 3 – 5 eV.

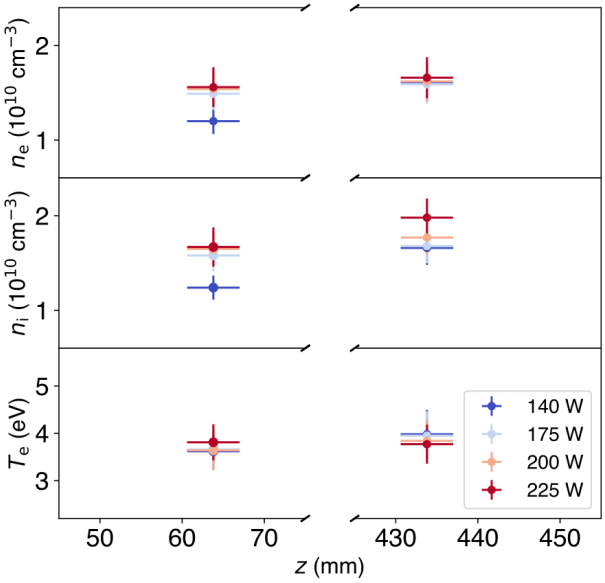

Figure 5. Comparisons between n_e, n_i and T_e measured at the outer cross and the inner cross for a range of absorbed powers at an operating pressure p_g = 1 Pa. The results show agreement between the plasma parameters in the two positions.

2023 JINST 18 P04008

where $P_{\rm abs}$ is the power absorbed by the plasma discharge, $A_{\rm eff}$ is the effective area for particle loss, and $\mathcal{E}_{\rm T}$ is the total energy loss per electron-ion pair created. The loss fluxes are

$$\Gamma_{\rm axial} = h_\ell n_0 u_{\rm B} \qquad \text{and} \qquad \Gamma_{\rm radial} = h_{\rm R} n_0 u_{\rm B} \tag{4.2}$$

for the axial and radial surfaces, respectively, and the edge-to-center density ratios in the intermediate pressure regime where $R, \ell \geq \lambda_{\rm i} \geq \frac{T_{\rm i}}{T_{\rm e}}(R, \ell)$ are [43]

$$h_\ell \equiv \frac{n_{s\ell}}{n_0} \simeq 0.86 \left(3 + \frac{\ell}{2\lambda_{\rm i}}\right)^{-1/2} \tag{4.3}$$

$$h_{\rm R} \equiv \frac{n_{s{\rm R}}}{n_0} \simeq 0.80 \left(4 + \frac{R}{\lambda_{\rm i}}\right)^{-1/2} \tag{4.4}$$

where $\lambda_{\rm i} = 1/m_{\rm g}\sigma_{\rm i}$ is the ion-neutral mean free path and $\sigma_{\rm i}$ is the combined ion momentum transfer cross section that includes both charge transfer and elastic collisions.

The total energy loss per electron-ion pair created is $\mathcal{E}_{\rm T} = \mathcal{E}_{\rm c} + \mathcal{E}_{\rm e} + \mathcal{E}_{\rm i}$ where the collisional energy lost per electron-ion pair created $\mathcal{E}_{\rm c}$ is given by

$$\mathcal{E}_{\rm c}(T_{\rm e}) = \mathcal{E}_{\rm iz} + \sum_{i=1}^{n} \frac{k_{{\rm ex},i}}{k_{\rm iz}} \mathcal{E}_{{\rm ex},i} + \frac{k_{\rm el}}{k_{\rm iz}} \frac{3m_{\rm e}}{M} T_{\rm e}\,, \tag{4.5}$$

and the electron kinetic energy lost to walls is $\mathcal{E}_{\rm e} = 2T_{\rm e}$, when the EEDF is Maxwellian, and the ion kinetic energy lost to walls is $\mathcal{E}_{\rm i} \approx \bar{V}_{\rm s}$, or simply the dc potential across the sheath. For the calculation of collisional energy lost per electron-ion pair created $\mathcal{E}_{\rm c}$ we use the electron impact ionization cross section from Straub et al. [44] and electron elastic and excitation cross sections for 25 excited levels from Hayashi [45].

For a uniform cylindrical plasma the particle balance is simply

$$\underbrace{n_{\rm g} n_0 k_{\rm iz} R^2 \ell}_{\text{ionization in the bulk plasma}} = \underbrace{(2\pi R^2 h_\ell n_0 + 2\pi R \ell h_{\rm R} n_0) u_{\rm B}}_{\text{ion loss to walls}} \tag{4.6}$$

which we rearrange to obtain

$$\frac{k_{\rm iz}(T_{\rm e})}{u_{\rm B}(T_{\rm e})} = \frac{1}{n_{\rm g} d_{\rm eff}} \tag{4.7}$$

where $d_{\rm eff} = \frac{1}{2} R\ell/(Rh_\ell + \ell h_R)$ is an effective plasma size. Given the atom density $n_{\rm g}$ (pressure) and $d_{\rm eff}$ (pressure, dimensions), we can estimate $T_{\rm e}$. For a 35 mm diameter tube with 300 mm length, at $p_{\rm g} = 0.5$ Pa the electron temperature is $T_{\rm e} = 4.7$ V, at 1 Pa $T_{\rm e} = 3.7$ V, and at 4 Pa $T_{\rm e} = 2.5$ V. Once the electron temperature is known, we can solve eq. (4.1) for the center particle density

$$n_0 = \frac{P_{\rm abs}}{A_{\rm eff} u_{\rm B} e \mathcal{E}_{\rm T}}\,. \tag{4.8}$$

For 200 W absorbed power the center electron density n_0 is 5.7×10^{11} cm^{-3} at 1 Pa. At 10 Pa n_0 increases to 1.1×10^{12} cm^{-3}.

Figure 6 shows the center particle density as a function of $P_{\rm abs}$ plotted alongside the peak electron and ion densities measured experimentally at 1 Pa using a Langmuir probe. We assume a

2023 JINST 18 P04008

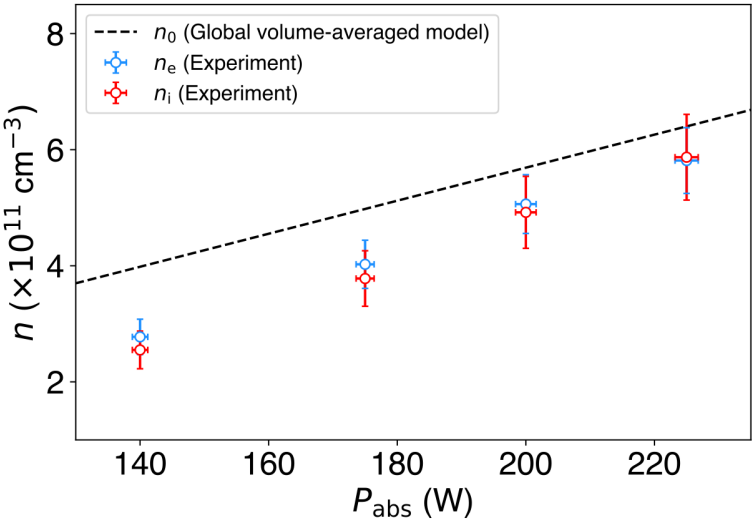

Figure 6. The center particle density n_0 obtained from the volume-average global model, compared with the densities obtained in the center of the coil from Langmuir probe measurements.

tube length of 300 mm for the calculation on the basis that the plasma conditions due to inductive coupling are expected to be decided by the particle and energy balances in the discharge region inside the coils. The ion loss flux is higher under the coils where power is coupled inductively to sustain the much-elevated plasma densities in this region. It is expected that the model calculation will overestimate the measured plasma densities because it does not account for the absorbed power consumed in sustaining the lower density plasma between the coils primarily via capacitive coupling. There is stronger agreement between the model and the measured values at larger P_{abs} where a larger fraction of the absorbed power is used to sustain the plasma by inductive coupling.

The volume-averaged model reasonably estimates the plasma density and temperature inside the coil, and provides predictions of how the plasma parameters will change when the operating pressure and applied power are modified.

5 Summary

A two-coil, meter-scale, table-top inductively-coupled argon plasma discharge has been deployed for use in high-energy-density science experiments. Using commercially-available components, it is possible to sustain a plasma in a vacuum chamber with volume approximately 1 L. Electron densities greater than 10^{11} cm^{-3} are measured when the argon fill pressure is 1 Pa.

The measured plasma parameters match estimates of commonly applied analytical models of inductive discharges. Typically these models treat the system as a transformer, with the inductive element taken as the primary circuit, and plasma taken as the secondary circuit [2, 19]. Applying a steady-state volume-averaged model [9–11] leads to estimates of electron temperature of $T_e = 3.0 - 5.0$ eV, and electron densities of $n_e = 10^{11} - 10^{12}$ cm^{-3}. In addition, we observe the trend that increased absorbed power leads to increased plasma electron densities, while the electron temperature does not change significantly.

2023 JINST 18 P04008

The modular design of the discharge makes it scaleable to longer lengths, and the inclusion of port crosses allows for diagnostic access. The design has been assembled using a commercially-available 1-kW power supply, making it an accessible option for studying physics involving meter-length plasmas in a University laboratory.

The discharge will be used in a high-energy-density science experiment at CERN's HiRadMat facility, in which beams of 440 GeV/c protons will be used to produce electron-positron pair beams, and their propagation through the plasma cell used to study collisionless electron-positron beam-plasma instabilities [27–30]. The experiment will study plasma processes relevant to the propagation and stability of relativistic pair plasmas associated with extreme relativistic phenomena such as Gamma-ray Bursts [46–48].

Acknowledgments

This project has received funding from the European Union's Horizon Europe Research and Innovation programme under Grant Agreement No 101057511 (EURO-LABS). We also acknowledge funding from AWE plc., and the Central Laser Facility (Science and Technology Facilities Council of the United Kingdom). U.K. Ministry of Defence © Crown Owned Copyright 2022/AWE.

References

[1] W. Hittorf, *Ueber die Electricitätsleitung der Gase*, *Annalen Phys.* **257** (1884) 90.

[2] J.J. Thomson, *On the discharge of electricity through exhausted tubes without electrodes*, *The London, Edinburgh, and Dublin Philosophical Magazine and Journal of Science* **32** (1891) 321.

[3] J.J. Thomson, *On the discharge of electricity through exhausted tubes without electrodes*, *The London, Edinburgh, and Dublin Philosophical Magazine and Journal of Science* **32** (1891) 445.

[4] J. Thomson, *The electrodeless discharge through gases*, *The London, Edinburgh, and Dublin Philosophical Magazine and Journal of Science* **4** (1927) 1128.

[5] V. Godyak, *Bright idea, radio-frequency light sources*, *IEEE Ind. Appl. Mag.* **8** (2002) 42.

[6] T. Lafleur and C.S. Corr, *Characterization of a radio-frequency inductively coupled electrothermal plasma thruster*, *J. Appl. Phys.* **130** (2021) 043304.

[7] J. Hopwood, *Review of inductively coupled plasmas for plasma processing*, *Plasma Sources Sci. Technol.* **1** (1992) 109.

[8] H.-C. Lee, *Review of inductively coupled plasmas: Nano-applications and bistable hysteresis physics*, *Appl. Phys. Rev.* **5** (2018) 011108.

[9] M.A. Lieberman and R.A. Gottscho, *Design of High-Density Plasma Sources for Materials Processing*, in *Plasma Sources for Thin Film Deposition and Etching*, M. Francombe and J. Vossen, eds., vol. 18 of *Physics of Thin Films*, Academic Press, New York, NY, U.S.A. (1994).

[10] M.A. Lieberman and A.J. Lichtenberg, *Principles of Plasma Discharges and Materials Processing*, 2nd edition, John Wiley & Sons, New York, NY, U.S.A. (2005).

[11] J.T. Gudmundsson and M.A. Lieberman, *Magnetic induction and plasma impedance in a cylindrical inductive discharge*, *Plasma Sources Sci. Technol.* **6** (1997) 540.

2023 JINST 18 P04008

[12] J.H. Keller, J.C. Forster and M.S. Barnes, *Novel radio-frequency induction plasma processing techniques*, *J. Vacuum Sci. Technol. A* **11** (1993) 2487.

[13] V.A. Godyak, R.B. Piejak and B.M. Alexandrovich, *The electron-energy distribution function in a shielded argon radiofrequency inductive discharge*, *Plasma Sources Sci. Technol.* **4** (1995) 332.

[14] V.A. Godyak, *Electrical and plasma parameters of ICP with high coupling efficiency*, *Plasma Sources Sci. Technol.* **20** (2011) 025004.

[15] V.A. Godyak, *Ferromagnetic enhanced inductive plasma sources*, *J. Phys. D* **46** (2013) 283001.

[16] H.U. Eckert, *The Hundred Year History of Induction Discharges*, in *Proceedings of the Second Annual International Conference on Plasma Chemistry and Technology*, H. Boenig, ed., pp. 171–202, Technomic Publishing, Lancaster, PA, U.S.A. (1986).

[17] N. Tesla, *Electric Discharge in Vacuum Tubes*, *The Electrical Engineer* **12** (1891) 14.

[18] K. MacKinnon, *On the origin of the electrodeless discharge*, *The London, Edinburgh, and Dublin Philosophical Magazine and Journal of Science* **8** (1929) 605.

[19] J. Tykocinski-Tykociner, *Measurement of current in electrodeless discharges by means of frequency variations*, *The London, Edinburgh, and Dublin Philosophical Magazine and Journal of Science* **13** (1932) 953.

[20] J. Amorim, H.S. Maciel and J.P. Sudano, *High-density plasma mode of an inductively coupled radio frequency discharge*, *J. Vacuum Sci. Technol. B* **9** (1991) 362.

[21] U. Kortshagen, N.D. Gibson and J.E. Lawler, *On the e - h mode transition in RF inductive discharges*, *J. Phys. D* **29** (1996) 1224.

[22] M.H. Clarkson, D.R. Keefer and B.E. Mathews, *Probe measurements in an electrodeless discharge.*, *AIAA J.* **4** (1966) 1850.

[23] T.B. Reed, *Induction-coupled plasma torch*, *J. Appl. Phys.* **32** (1961) 821.

[24] S.M. Rossnagel, A. Sherman and F. Turner, *Plasma-enhanced atomic layer deposition of Ta and Ti for interconnect diffusion barriers*, *J. Vacuum Sci. Technol. B* **18** (2000) 2016.

[25] H.B. Profijt, M.C.M. van de Sanden and W.M.M. Kessels, *Substrate biasing during plasma-assisted ALD for crystalline phase-control of TiO2 thin films*, *Electrochem. Solid-State Lett.* **15** (2011) G1.

[26] I. Efthymiopoulos, D. Grenier, M. Meddahi, P. Trilhe, S. Evrard, H. Vincke et al., *HiRadMat: a new irradiation facility for material testing at CERN*, Tech. Rep., CERN-ATS-2011-232, CERN, Geneva, Switzerland (2011).

[27] C.D. Arrowsmith et al., *Generating ultradense pair beams using 400 GeV/c protons*, *Phys. Rev. Res.* **3** (2021) 023103 [arXiv:2011.04398].

[28] S.A. Bludman, K.M. Watson and M.N. Rosenbluth, *Statistical mechanics of relativistic streams. II*, *Phys. Fluids* **3** (1960) 747.

[29] R. Lee and M. Lampe, *Electromagnetic Instabilities, Filamentation, and Focusing of Relativistic Electron Beams*, *Phys. Rev. Lett.* **31** (1973) 1390.

[30] B.B. Godfrey, W.R. Shanahan and L.E. Thode, *Linear theory of a cold relativistic beam propagating along an external magnetic field*, *Phys. Fluids* **18** (1975) 346.

[31] J.-I. Sakai, R. Schlickeiser and P.K. Shukla, *Simulation studies of the magnetic field generation in cosmological plasmas*, *Phys. Lett. A* **330** (2004) 384.

2023 JINST 18 P04008

[32] M.V. Medvedev and A. Spitkovsky, *Radiative cooling in relativistic collisionless shocks. Can simulations and experiments probe relevant GRB physics?*, *Astrophys. J.* **700** (2009) 956 [arXiv:0810.4014].

[33] D.M. Danielsson, J.T. Gudmundsson and H.G. Svavarsson, *Effect of hydrogenation on minority carrier lifetime in low-grade silicon*, *Phys. Scripta* **141** (2010) 014005.

[34] M.T. Sultan, J.T. Gudmundsson, A. Manolescu, T. Stoica, M.L. Ciurea and H.G. Svavarsson, *Enhanced photoconductivity of embedded SiGe nanoparticles by hydrogenation*, *Appl. Surf. Sci.* **479** (2019) 403.

[35] J.G. Laframboise, *Theory of Spherical and Cylindrical Langmuir Probes in a Collisionless, Maxwellian Plasma at Rest.*, Ph.D. thesis, University of Toronto, Canada (1966).

[36] G. Narasimhan and C. Steinbrüchel, *Analysis of Langmuir probe data: Analytical parametrization, and the importance of the end effect*, *J. Vacuum Sci. Technol. A* **19** (2001) 376.

[37] J.E. Allen, R.L.F. Boyd and P. Reynolds, *The collection of positive ions by a probe immersed in a plasma*, *Proceedings of the Physical Society. Section B* **70** (1957) 297.

[38] S. Klagge and M. Tichý, *A contribution to the assessment of the influence of collisions on the measurements with Langmuir probes in the thick sheath working regime*, *Czech. J. Phys.* **35** (1985) 988.

[39] M.J. Druyvesteyn, *Der niedervoltbogen*, *Zeit. Phys.* **64** (1930) 781.

[40] F. Magnus and J.T. Gudmundsson, *Digital smoothing of the Langmuir probe I-V characteristic*, *Rev. Sci. Instrum.* **79** (2008) 073503.

[41] M. Hopkins, *Langmuir probe measurements in the gaseous electronics conference rf reference cell*, *J. Res. Natl. Inst. Standards Technol.* **100** (1995) 415.

[42] J.T. Gudmundsson, *On the effect of the electron energy distribution on the plasma parameters of an argon discharge: a global (volume-averaged) model study*, *Plasma Sources Sci. Technol.* **10** (2001) 76.

[43] V.A. Godyak, *Soviet Radio Frequency Discharge Research*, Delphic Associates, Falls Church, VA, U.S.A. (1986).

[44] H.C. Straub, P. Renault, B.G. Lindsay, K.A. Smith and R.F. Stebbings, *Absolute partial and total cross sections for electron-impact ionization of argon from threshold to 1000 eV*, *Phys. Rev. A* **52** (1995) 1115.

[45] M. Hayashi, National Institute for Fusion Science of Japan, Gifu-Ken, Japan (2003).

[46] M.V. Medvedev and A. Loeb, *Generation of magnetic fields in the relativistic shock of gamma-ray burst sources*, *Astrophys. J.* **526** (1999) 697 [astro-ph/9904363].

[47] R. Shaisultanov, Y. Lyubarsky and D. Eichler, *Stream instabilities in relativistically hot plasma*, *Astrophys. J.* **744** (2012) 182 [arXiv:1104.0521].

[48] L.O. Silva, R.A. Fonseca, J. Tonge, J.M. Dawson, W.B. Mori and M.V. Medvedev, *Interpenetrating plasma shells: Near-equipartition magnetic field generation and non-thermal particle acceleration*, *Astrophys. J. Lett.* **596** (2003) L121 [astro-ph/0307500].

2023 JINST 18 P04008